Beam Current and Target Density Normalization in E952 ($^{12}\mathrm{C}(\alpha,\gamma)^{16}\mathrm{O}$) at DRAGON

Wolf-Rüdiger Hannes
University of Konstanz, Germany

DRAGON Research Group, TRIUMF
Vancouver B.C., Canada

External Supervisor: Dr. Lothar Buchmann
Internal Supervisor: Prof. Dr. Günter Schatz

February 25th, 2005

Contents

1 Theory

1.1 Nuclear Capture Reactions

In the final stages of stellar evolution the increasing temperature allows the occurence of various nuclear capture reactions. Heavy elements are created from lighter ones, a process called nucleosynthesis, and hugh amounts of energy are irradiated into space. Many types of these reactions can be investigated with DRAGON, the Detector for Recoils And Gammas Of Nuclear reations.

Most of the astrophysically important capture reactions involve proton- or α-capture. With (α,γ)-reactions, an atomic nucleus and an α-particle merge into one single heavier nucleus. The binding energy, corresponding to the reactions Q-value, is released in the form of γ-rays. The energy of the emitted γ-rays is the sum of the Q-value and the proportion of kinetic energy transformed into excitation energy during the inelastic collision. Except for direct capture reactions, nuclear reactions can be considered to consist of two stages: the formation of a compound nucleus, and its decay into reaction products. In the reaction $^{12}\mathrm{C}(\alpha,\gamma)^{16}\mathrm{O}$, the compound nucleus is an excited oxygen nucleus.

Even at typical explosive stellar temperatures the reactants are kept far apart by the repellent Coulomb force between the capture nucleus and hydrogen/helium. Reactions take place via tunneling processes through the Coulomb barrier into the short range of attractive strong forces. Nuclei in a stellar sphere with temperature T posess a Maxwell-Boltzmann energy distribution ($\propto exp(-E/k_BT)$) with the most likely energy $E = 2k_BT$. However, nuclear reactions between charged particles rarely occure at $E = 2k_BT$, because the probability for tunneling through the Coulomb barrier, which increases with E, is too small. The convolution of the Maxwell-Bolzmann distribution with the quantum-mechanical tunneling function results in a peak at an energy E_0, which is generally much larger than k_BT. In this energy region, called Gamow window, the highest number of compound nuclei are formed.

A compound nucleus naturally possesses a set of quasi-stationary states with finite lifetimes. If the energy of an incident particle (measured in the center-of-mass system, cms) is close to the energy of one of the nuclear compound levels, then the probability of producing the compound nucleus becomes particularly large. The energy levels hence appear as resonance maxima in the reaction rates. These rates are also affected by interferences between the resonances and by the direct capture process, which can be considered as an individual interaction of the incident particle with separate nucleons of the target nucleus.

The rates of nuclear capture reactions, conveniently described in terms of a cross section $\sigma(E)$, are very small: usually $\sigma(E)$ is in the range of mbarn, where 1 barn = 10^{-24} cm^2. In order to measure reaction cross sections, the very small amount of reaction products, called recoils, has to be separated

from a high energy beam of particles passed through a target. DRAGON is conceived for the technique of inverse-reaction kinematics, which is necessary for the separation of recoils e.g. from the $^{12}C(\alpha,\gamma)^{16}O$ reaction. That is, heavy ions rather than protons or α-particles are accelerated, whereas the target consists of hydrogen or helium gas. Recoils hence continue in a forward direction along with the incident beam and are sufficient fast to be detected. The beam to recoil energy ratio is the inverse of their mass ratio, because of the conservation of momentum at inelastic processes and the very little momentum of the γ-rays. With a combination of two magnetic and two electric dipoles, DRAGON's separation capability is about 10^{-15}. Another advantage is the simultaneos detection of the γ-rays escaping from the target cell wherein the nuclear reactions take place.

In order to calculate reaction rates, one must know the number of recoils, the beam current through the target, and the target density. The goal of this work project was to enable the calculation of the beam current through the target cell by means of two monitors detecting elastically scattered target atoms. This has been carried out for the data of $^{12}C(\alpha,\gamma)^{16}O$ measurements.

1.2 The Reaction $^{12}C(\alpha,\gamma)^{16}O$

The reaction $^{12}C(\alpha,\gamma)^{16}O$ takes place during the helium burning phase. Stars in this development phase are called 'Red Giants', since the hydrogen burning shell expands due to the heating from the helium burning core. Its surface cools down and causes the red color. Helium burning begins with reactions among helium nuclei forming ^{12}C in the so-called triple-α process. In turn, created carbon nuclei can radiatively capture another helium nucleus to form ^{16}O. These two reaction rates determine the amounts of ^{12}C and ^{16}O after helium burning. The $^{12}C/^{16}O$ ratio itself strongly influences the abundances of heavier elements built from these nuclei. [1]

In fig. 1 an energy level diagram of oxygen is displayed along with the Q-value of $^{12}C(\alpha,\gamma)^{16}O$, the Gamow window and the energy range investigated in this experiment. Helium burning temperatures of about 10^8 K correspond to a Gamow-window at E_{cm}=0.3 MeV. Though there is no level in this energy region, the large abundance of oxygen, which is only created in stars, indicates that $\sigma(E_{cm} = 0.3\text{MeV})$ does not vanish completely. Probably the reaction rates are influenced slightly by the low-energy tail of the broad 2.42 MeV resonance (E_x=9.585 MeV) and strongly by the high-energy tails of two subthreshold resonances at -45 and -245 keV (1- and 2+ states). These resonances also interfere among each other and with the direct capture process. However, the cross sections in this energy region are too small for technical detection capabilities. Proceeding to higher energies, $\sigma(E)$ increases because of nearby resonances. Measurements of cross sections at higher energies can provide information on the reaction mechanisms involved in the capture process. Then extrapolations to the stellar energy region

[1] Further information on the key reaction $^{12}C(\alpha,\gamma)^{16}O$ can be found in Ref. [1] and [2].

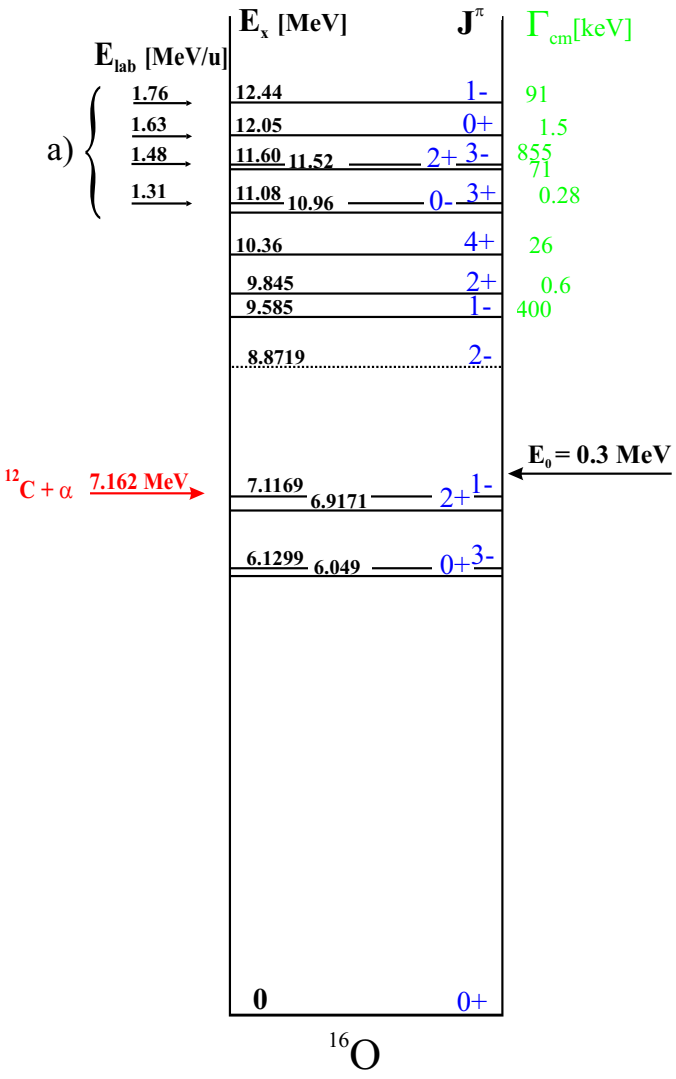

Figure 1: The Energy Scheme of Oxygen Nuclei. Shown as well are the α-threshold at 7.162 MeV, the Gamow-window at E_0 and the energy range investigated in this experiment (a). The energies of some resonances in the investigated range are transformed to laboratory energies of accelerated ^{12}C ions (useful for a comparison with fig. 4 and 7).

might become possible.

The reaction $^{12}\mathrm{C}(\alpha,\gamma)^{16}\mathrm{O}$ is a difficult experiment to do with DRAGON, which was originally concipated for (p,γ)-reactions of short-lived radioactive nuclei. Because of the small reaction rates the runs usually last several hours, which makes an accurate measurement of the beam current particularly important.

1.3 Elastic Scattering and the Differential Cross Section

For low energies ($E_{lab} < 0.6\frac{\mathrm{MeV}}{\mathrm{u}}$ for inverse kinematics) the rate of the scattering process $^{12}\mathrm{C}(\alpha,\alpha)^{12}\mathrm{C}$ is well described by the Rutherford cross section. However, as the energy increases, tunneling processes happen more frequently and compound nuclei are formed. Rather than deexcitating to ground-state oxygen, most of these nuclei decay by another tunneling process so that both initial nuclei are retrieved. This process (called compound elastic scattering) makes the scattering rates, described in terms of a differential cross section, dependend on the nuclear structure of oxygen.

The differential cross section $\frac{d\sigma}{d\Omega}(\theta, E)$ describes the probability of a certain collision event, usually in the center-of-mass (cm) system of the collision (i.e. $d\sigma, d\Omega, \theta$ and E are measured in cms). For our case of detecting scattered target atoms (rather than beam particles), $\frac{d\sigma}{d\Omega}(\theta, E)$ can be illustrated as follows: Consider one atom as a target for a monoenergetic particle beam of energy E. Then $d\sigma$ is a certain area (perpendicular to the beam-axis) where those incident particles enter, that collide with target atoms scattered into the solid angle $d\Omega$ at a certain scattering angle θ.

As described in chapter 2.3, we use the elastic monitors to detect elastically scattered target atoms rather than beam particles. In this case, θ is the scattering angle of a target atom after a collision.

The differential cross section can be calculated by

$$\frac{d\sigma}{d\Omega}(\theta, E) = \frac{1}{I_0} \cdot \frac{1}{n_{target}} \cdot \frac{dN}{d\Omega} \ , \tag{1}$$

where

- I_0 is the integrated particle current of the incident beam,
- n_{target} is the number of target atoms per area in the intersection of beam and focused volume, and
- $\frac{dN}{d\Omega}$ is the number of scattered particles into the solid angle dΩ at the scattering angle θ.

In this formula, effects like multiple scattering, beam attenuation and energy loss in the target are disregarded, and hence it presupposes small target thickness.

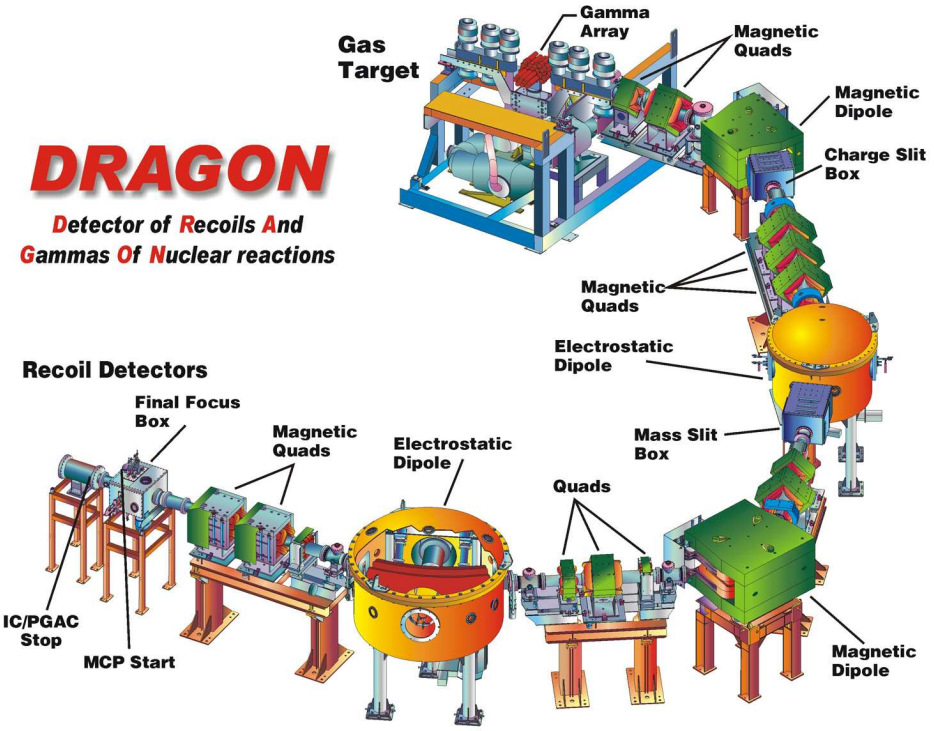

Figure 2: Schematic 3D view of DRAGON

2 Experimental Setup

The description of the setup starts at the accelerator and then follows the beam line through the target and the 21 m long recoil separator to the end detectors. Basically the devices used in this project are specified. The data aquisition is also addressed. A nice drawing of DRAGON[2] is shown in fig. 2.

2.1 Particle Acceleration at the ISAC Facility

Radioactive beams at ISAC[3] (Isotope Separator and ACelerator) are produced with an On Line Isotope Separation technique (ISOL): high energy protons from TRIUMF's main cyclotron irradiate a specific target and produce a large number of radionuclides via nuclear reactions. The desired products are transfered into an ion source and enter the acceleration beam line of ISAC.

The accelerator includes a Radio Frequency Quadrupole (RFQ), a stripper foil (as charge state booster) and a variable energy drift tube linac (a linear accelerator) to accelerate ions to a final energy from 0.15 to 1.8 $\frac{\text{MeV}}{\text{u}}$.

[2]More detailed descriptions of parts of the facility can be found on the DRAGON website http://dragon.triumf.ca/results.html, especially [3] and [4].

[3]For further information see [5] or http://isacwserv.triumf.ca/

In this experiment we deal with stable ^{12}C-beam. Stable beams are produced with the OffLine Ion Source OLIS. The currents of ^{12}C-ions delivered to DRAGON are typically of the order of 100 enA.

2.2 Gas Target

The target gas, in this experiment helium of a few Torr, resides in a windowless cell, i.e. there are no foils covering the beam apertures. Foils are avoided for different reasons: the deposit of beam particles on a foil can result in additional reactions, and the modification of the beam by further processes (like scattering, charge changing processes and energy straggling) would deteriorate the recoil separation.

The target cell is contained in an evacuated box, of which a cross section is shown in fig. 3. Because of gas escaping through the beam apertures (of 6 and 8 mm diameter at upstream and downstream side, respectively), the nearby beam tubes have to be evacuated with a differential pumping system (visible in fig. 2). The target gas is recirculating, but usually the pressure slowly decreases as long as no gas is refilled from a tank. The pressure in the target cell is measured by a capacitance manometer (SMGC). The angular acceptance for recoils is ± 20 mrad, which is determined by the increasing diameters of the beam tubes within the differential pumping system. On either side of the target system, there are Faraday cups (FC4 upstream and FC1 downstream of the target), that can be put into the beam line for an instantaneous measurement of the beam current.

Capture reactions as well as elastic scattering processes are caused by interactions between projectile and target nuclei. But there are also interactions between the electron shells of projectiles and target atoms. This has several effects, e.g. beam deceleration and energy straggling. Also, projectiles might lose (or capture) electrons during those interactions. These charge changing processes cause, that beam and recoils emerge from the target in many different charge states. The fractions of the charge states, called the charge state distribution (CSD), depends on the beam energy and the target density.

2.3 Elastic Monitors

Two Silicon Surface Barrier (SSB) detectors, also visible in fig. 3, are mounted into the target cell and collimated to view a central portion of the beam line in the gas. These so-called elastic monitors detect elastically scattered target atoms (helium atoms). The telescopes have a mutual collimator (parallel to the beam line) and are tilted at 57° (EM1) and 30° (EM2) with respect to the beam axis. Because the maximum scattering angle of carbon at the collision ^{4}He(^{12}C,^{12} C)^{4}He is 19.4°, beam ions don't hit the detectors (without multiple scattering). The detectors are connected to modular electronics with a prescaler, which posesses a certain dead time after each detection event.

2.4 γ-Detector Array

The target box is surrounded by an array of 30 scintillation detectors (bismuth germinate, BGO) for the detection of γ-radiation from the nuclear fusion reactions.

2.5 Recoil Separator

A complex system of bending magnets, electrostatic dipoles and focusing magnets performs the separation of the reaction product nuclei from the beam particles which are about $10^{12}-10^{15}$ times more numerous. Quadrupoles are employed for steering the beam through the separator and sextupols for focusing the beam at the selection slits. The recoil filter consists of two magnetic and two electrostatic dipoles.

A magnetic field separates ions according to their momentum to charge ratio. As described in chapter 1.1, the momentum of beam and recoil particles fairly agrees, so that one certain charge state is selected by the first magnetic dipole (MD1). This selection is made by means of a set of horizontal and vertical slits. All undesired charge states are stopped within the charge slit box. Subsequent to the charge slits, there is another Faraday cup

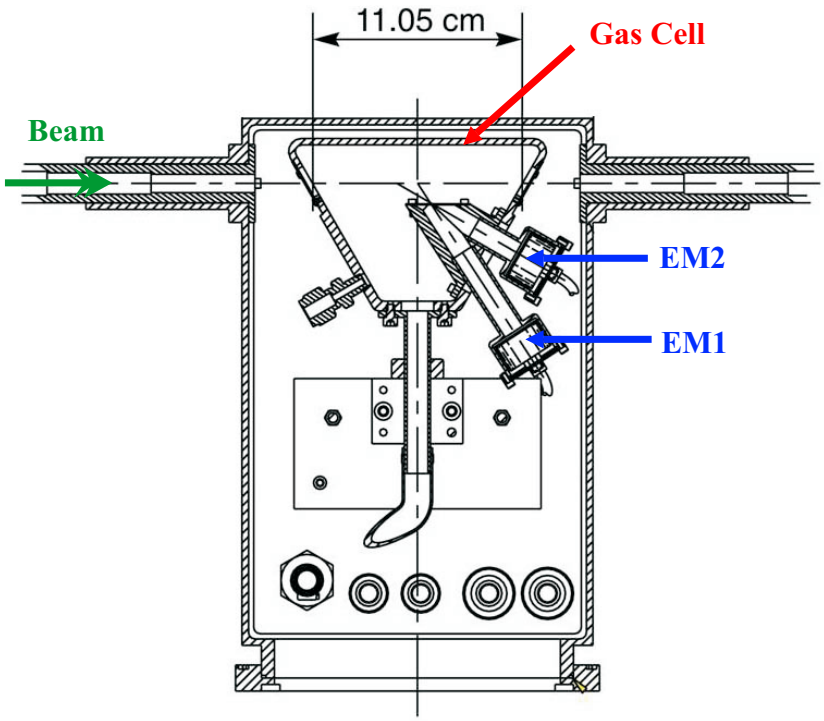

Figure 3: Profile of Target Box with Windowless Gas Cell and Elastic Monitors

(FCCH) for reading the beam current of the selected charge state.

The energy to charge ratio is the separation criterium in an electric field, which results in mass separation at the electric dipoles. If the first electric dipole ED1 is applied with a voltage appropriate for recoil separation, then the beam particles, possessing higher energy and hence experiencing a smaller deflection, can be detected with a Faraday cup. This Faraday cup (FCM2) sits off-axis next to the mass slits within the mass slit box and provides permanent measurement of the beam current at this location.

The subsequent dipoles (MD2 and ED2) are required for further extraction of leaky beam among the recoils.

2.6 Recoil Detectors

Finally, the recoils are detected with a double-sided silicon strip detector (DSSSD), providing information not only about their number but also about their energy and lateral position. In front of the DSSSD, a multi-channel plate (MCP) can be used for time-of-flight measurements.

2.7 Data Acquisition and Analysis Programs

The MIDAS standard data acquisition controls the data acquisition of DRAGON.

From the detector readout, in the form of event-by-event data, an Analyzer program increments histograms, which can be displayed on-line or off-line with the CERN package PAW++ (physics analysis workstation).

Setup parameters of DRAGON are written to files by a command-line-interpreter run on the on-line data base (odb).

MIDAS can be used to display history recordings of Faraday cups, slit widths and positions, dipoles etc.

3 Beam Current and Target Density Normalization

As described above, the beam flux is measured with a Faraday cup at a location where the recoils are separated. However, there is always the risk that FCM2 gives wrong values of the beam current, e.g. in the case of beam loss downstream of the target. The use of the elastic monitors could be more reliable, since they provide a quantity of the beam current in the target cell itself.

The differential cross section of the elastic scattering process $^{12}\mathrm{C}(\alpha,\alpha)^{12}\mathrm{C}$ has been measured in other experiments, in which a carbon foil is striked by a beam of α-particles. In the following, this data for $\frac{d\sigma}{d\Omega}(\theta, E)$ is referred to as the theoretical data (because it is calculated with the R-matrix theory, where the fit parameters have to be taken from experimental data).

By means of this scattering data, we can calculate the beam current through the target gas from the number of ^{4}He-atoms, elastically scattered into one of the elastic monitors. However, this method is only feasible, if the theoretical curve can be generated from the experimental data. As described in the next section, this could not be achieved by a simple evaluation. Major deviations and spreadings were visible in the elastic scattering spectra (plots of $\frac{d\sigma}{d\Omega}$ over energy E). The goals of this study were to normalize the elastic scattering data in respect of beam current and target density, and to figure out the reasons for the deviations.

3.1 How to Measure Differential Cross Sections

According to eq. 1, a spectrum of $\frac{d\sigma}{d\Omega}(E)$ can be calculated from the quantities E, I_0, n_{target} and $\frac{dN}{d\Omega}$ (the scattering angle θ is determined by the detector position). Now we look for applicable measurement quantities.

For gas pressures of only a few Torr, we can describe the target density n_{target} accurately in terms of the pressure p in the target cell:

$$n_{target} = \frac{N_{target}}{\text{area}} = \frac{N_{target}}{\text{volume}} \cdot l_{target} = \frac{p}{k_B T} \cdot l_{target} \tag{2}$$

Here l_{target} is the length of the beam line fraction within the detector focus (determined by the collimator sizes). The second transformation in eq. 2 represents the ideal gas law with pressure p, temperature T and boltzmann factor k_B.

Now we can write the differential cross section as

$$\frac{d\sigma}{d\Omega}(\theta, E) = \frac{1}{I_0} \cdot \frac{N}{\Omega} \cdot \frac{1}{p} \cdot l_{target} \cdot k_B T, \tag{3}$$

where N is the count number of the detector (positioned at a lab-angle corresponding to θ and posessing a solid angle Ω).

In order to determine Ω, it is necessary that l_{target} is small compared with the detector size and the telescope length. For the gas target this criterium

could be met by very small collimators, but those would drastically reduce the detection rates. Because the collimators in our setup allow scattering angles of about $\pm 6^\circ$ (in respect to the telescope angle) it is very difficult to calculate absolute values for $\frac{d\sigma}{d\Omega}(\theta, E)$ (without simulations).

However, we don't need absolute values (because we have the comparative value FCM2) and restrict to the quantity

$$\frac{N}{I_0 \cdot p} \ ,$$

which is proportional to $\frac{d\sigma}{d\Omega}$, if the beam geometry is fixed and the gas temperature is constant.

In a simple evaluation the quantities required for the calculation of $\frac{d\sigma}{d\Omega}(\theta, E)$ were obtained as follows:

- E: the energy of incident beam, measured as described in sect. 3.4,
- N: the peak of elastically scattered α-particles in the "$E \times counts$"-spectrum is extracted from a low-energy background and the obtained number multiplied by both the prescaler setting and a dead time factor,
- I_0: the integrated beam current measured with the current integrator of FCM2,
- p: the mean value of two pressure values recorded at the start and the end of each run.

The results, shown in fig. 4, are not consistent with the theoretical data. The beneficial efforts made to improve these spectra are described in the following chapters.

Information about the reasons of the deviations can be obtained by looking at the ratio of EM1 and EM2 counts, because this is independent from uncertainties in the beam current or the target density. Because it fairly agreed with the theoretical data, the major error sources were suspected in the FCM2 and pressure data.

3.2 Beam Current

The current at FCM2 is not necessarily proportional to the current through the target, because the fraction of the charge state selected with MD1 depends on the beam energy E and the target pressure p - two quantities which are varied in $^{12}\mathrm{C}(\alpha,\gamma)^{16}\mathrm{O}$ measurements.

The charge state distribution of the beam particles is usually different from that of the recoils. Thus, the ratio of recoil to beam particles downstream of MD1 is susceptible to charge state distributions. However, this undesired effect on the recoil spectra is quite complicated, because it even depends on the location of the reaction resonance in the target cell.

There is also the possibility of beam loss between the target and ED1, or the risk that some beam particles don't hit FCM2. (The beam loss in

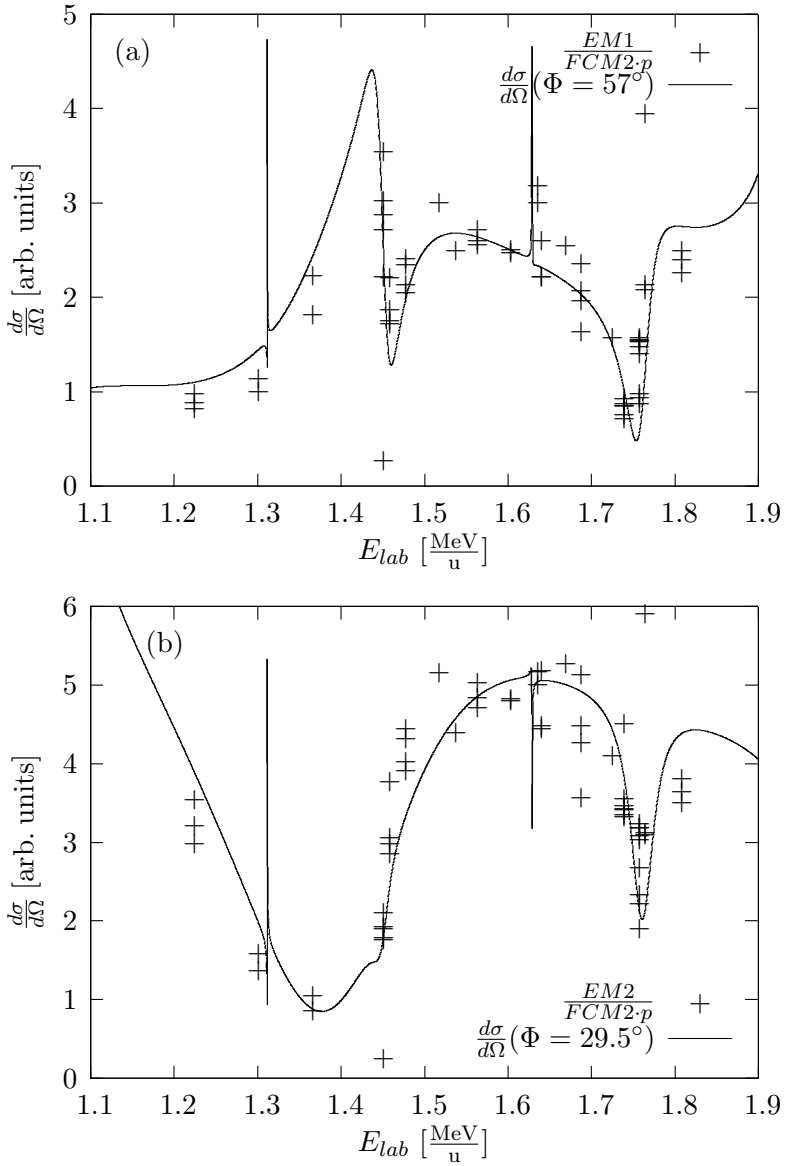

Figure 4: Elastic scattering rates for EM1 (a) and EM2 (b) obtained with a simple evaluation. The scattering angles used for the calculation of $\frac{d\sigma}{d\Omega}(\theta, E)$ with an R-Matrix program correspond to the direction of the telescope axis. The experimental results are scaled to the theoretical lines. Statistical errors (from the number of counts) are not shown since they are negligible compared to experimental inaccuracies.

the target gas due to elastic scattering is negligible.) If the elastic scattering rates would be fairly consistent with the beam current detected by FCM2, then the erranous runs could be pointed out by looking at the scattering spectra. In order to obtain this consistency, the pressure and energy dependence of the charge state fraction has to be regarded.

The charge state of the incoming carbon beam is 3+ for $E_{lab} < 1.75 \frac{\mathrm{MeV}}{\mathrm{u}}$ and is switched to 4+ for higher energies. With the magnetic dipoles, the charge state 6+ is selected, and its fraction $CSF_{6+}(p, E)$ is expected to increase both with p and E. In a first evaluation I have assumed a linear pressure dependence while neglecting the energy dependence, but this method did not result in reliable elastic-scattering spectra. Accurate data for $CSF_{6+}(p, E)$ was required.

During charge changing processes, the projectile drops off or picks up one or more electrons. The cross sections for these processes $\sigma_{q,q\pm1}$ depend in a complicated way on the sort of atoms (ordinary numbers Z_{proj}, Z_{target}) and the beam energy E. There is no formula for $\sigma_{q,q\pm1}(E, Z_{proj}, Z_{target})$, that is valid in a certain range of these variables. Applicable literature values were not available either.

Another attempt was to derive $CSF_{6+}(p, E)$ from the Faraday cup data in the run sheets (or MIDAS), since the beam current is usually measured with FC4 and FC1 at the start end end of each run. But the current at FC1 (measured in enA) cannot be transformed into a particle current if the charge state distribution is unknown. At FC4 there is only one charge state, but the current measured at this location is not accurate enough because of beam loss at the front collimator of the target cell. A consistent function for $CSF_{6+}(p, E)$ could not be derived from the available Faraday cup data.

3.2.1 Measurements of Charge State Distributions

The only solution was an explicit measurement of the charge state fraction $CSF_{6+}(p, E)$. In order to obtain this proportion, the fractions of all occupied charge states must be measured for each desired combination of p and E. CSD measurements have been carried out for a C^{3+}- and a O^{4+}-beam of various energies striking the helium target of various pressures. The pressure dependence of the CSD is plotted for each two beam energies of carbon and oxygen in fig. 5, while the whole data is listed in appendix B. The CSD of the oxygen beam can be used for refining the recoil spectra of $^{12}\mathrm{C}(\alpha, \gamma)^{16}\mathrm{O}$ measurements.

The procedure for one CSD measurements (one certain pressure and energy) is as follows: each of the most populated charge states (4+,5+,6+ for Carbon) is selected with MD1 so that its beam is centered at the charge slits. Then the current of this charge state can be detected with FCM2 (provided that ED1 is set for recoil selection). Readings of FC1 can provide cross-checks, since the sum of all charge states adds up to the beam current upstream of MD1.

For sufficient low target pressures, the proportion of higher charge states

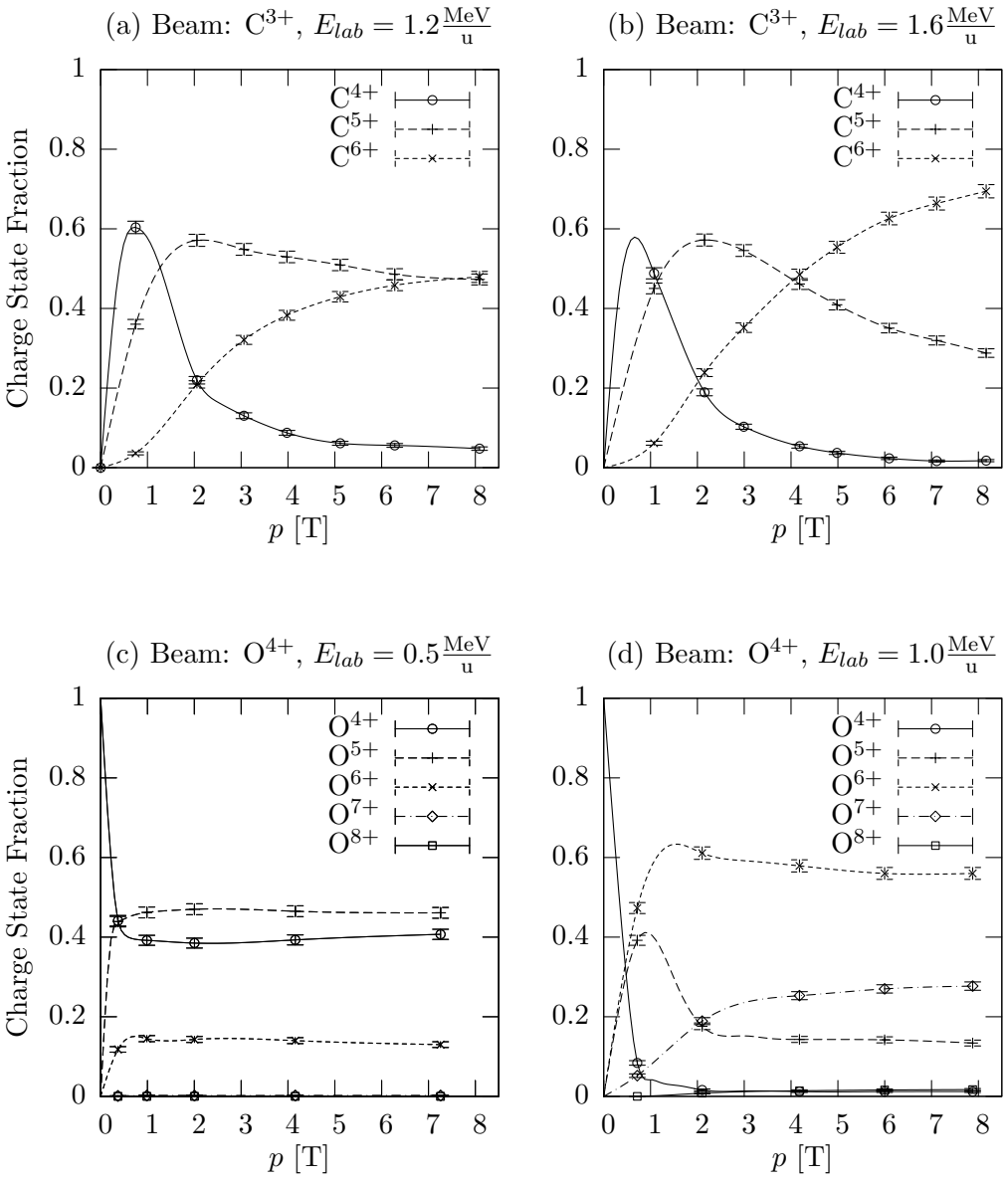

Figure 5: Some CSD-results for carbon (a+b) and oxygen (c+d). The curves are to guide the eye.

increases with p, because the cross sections for electron loss dominate those for electron capture. However, at a certain target thickness, electron loss and capture cancel out each other and the cross sections become independent of the target thickness. Thus, the charge state fractions become constant as well. This so-called equilibrium region is visible in fig. 5c). The equilibrium CSD of the oxygen beam with $E_{lab} = 0.75\frac{\mathrm{MeV}}{\mathrm{u}}$ could be compared with former data (Ref. [6]), and a good agreement was found.

3.3 Target Density

Of course it is difficult to keep a constant gas pressure in a windowless target cell. For helium gas of 3.5T $\leq$ p $\leq$ 4T, the target pressure decreases at a rate of about 0.05 T/hour. The manometer SMGC, recording the target pressure, is not included in DRAGONs Data Acquisition System. Available was only the data in the run sheets, read at the start and end of each run. However, its mean values do not provide accurate average pressures, because most $^{12}\mathrm{C}(\alpha,\gamma)^{16}\mathrm{O}$ runs span several hours and sometimes the target gas is refilled during runs. Fortunately, SMGC is recorded (at 5 min-intervals) with TRAR (TRIUMF Ascii Archiver); the Ascii files can be found in the databases of the ISAC facility. The data has been extracted with a proper C^{++}-program and average pressures for each run have been calculated. The effect on the elastic spectra was positive because of the contraction of data points at the same energy value.

3.4 Beam Energy

During their passage through the target gas, beam ions are decelarated mainly as a result of interactions between the electron shells. These inelastic collisions also cause ionization (see chapter 3.2) and excitation of atoms. The latter effect makes it possible to look at the beam profile with a CCD-camera focused from the downstream side into the target gas.

By means of the first magnetic dipole, the energy of the beam behind the target can be determined by finding the MD1 field which puts the beam on-axis at the charge-selection slits. This is usually done for several target pressures, and the approximately straight line is extrapolated to a pressure of 0 Torr. The result corresponds to the beam energy in front of the target.

The stopping of ions into matter can be calculated with the program SRIM ([8]), which uses a quantum-mechanical treatment of ion-atom collisions. The energy loss ΔE of ^{12}C-ions up to the center of the target cell has been calculated with SRIM for several beam energies and target pressures. The results in the relevant ranges ($E_{in} = 1.0\ \frac{\mathrm{MeV}}{\mathrm{u}}$ .. $1.8\ \frac{\mathrm{MeV}}{\mathrm{u}}$ and $p = 3..4.5$ T) can be well approximated by a linear function:

$$\frac{\Delta E}{\mathrm{keV/u}} = 0.7 \cdot \frac{p}{\mathrm{T}} - 0.793 \cdot \frac{E}{\mathrm{MeV/u}} + 1.16\ . \tag{4}$$

The difference of beam energy between the two sections seen by $EM_{1,2}$ has

not been considered, since the energy spread of the ISAC beams is about 1 $\frac{\text{keV}}{\text{u}}$ (FWHM).

3.5 Detected Elastic Scattering Rates

In the elastic monitor spectra 'count number versus particle energy' (these spectra can be displayed with PAW++), the number of scattered He atoms can be extracted from background by integrating over a peak. The spectra of one $^{12}\text{C}(\alpha,\gamma)^{16}\text{O}$ run are shown in fig. 6. Only the small tail of low energy background (caused perhaps by multiple scattering or scattered electrons) overlaps with the peak.

The obtained count number has to be divided by a factor determined by the dead time of the electronics. This factor can be calculated with the ratio of heavy ions acquired and presented, both numbers documented in the online database (.odb) files.

3.6 Improved Results

With the several refinements described in the previous sections, we obtained much better elastic scattering spectra (see fig. 7), but they still didn't agree with the theoretically expected curve (dashed line). In order to figure out the reasons, the ratio of experimental and theoretical data has been plotted over various quantities, e.g. the length of the run, but no further experimental inaccuracy could be found.

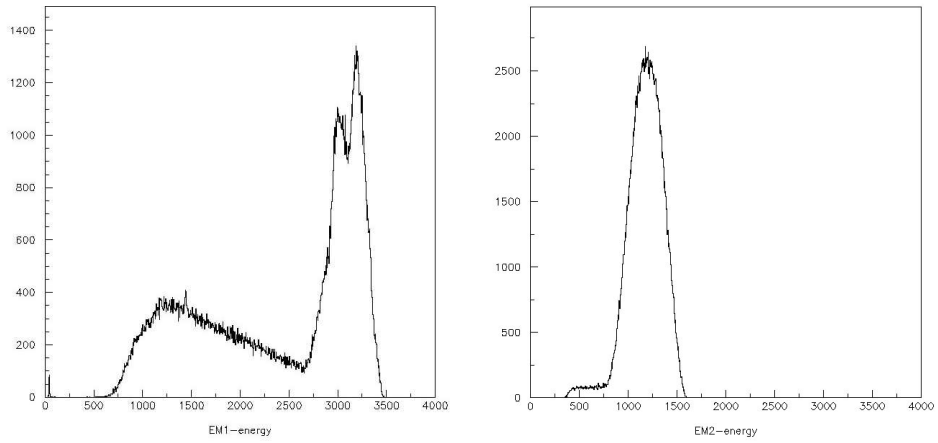

(a) EM1 (b) EM2

Figure 6: Elastic Monitor Spectra (count number versus energy) of one $^{12}\text{C}(\alpha,\gamma)^{16}\text{O}$ Run (Run# 12114, $E = 1.688\frac{\text{MeV}}{\text{u}}$). The background could arouse from multiple scattering of ^{12}C and ^{4}He particles and/or from scattered electrons. The double peak structure for EM1, increasing in intensity with beam energy E, has been inexplicable; a possible explanation is discussed in sect. 3.7.2.

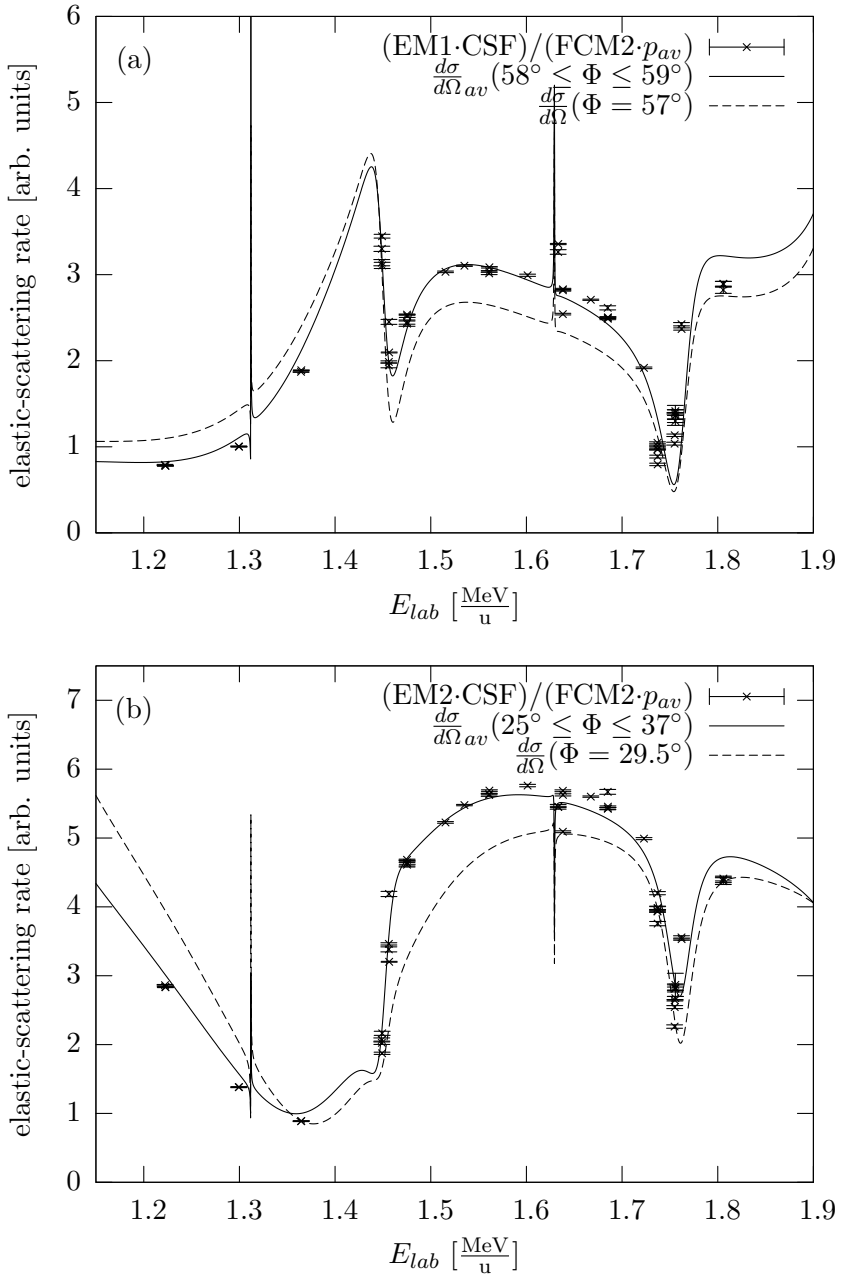

Figure 7: Rates of elastic-scattering with the improvements described in chapters 3.2 - 3.4. For all data above 1.75 $\frac{\text{MeV}}{\text{u}}$, the CSF is unknown, which results in some deviations. The dashed theoretical lines are the same as in fig. 4. The solid lines are cross sections folded with a function for the angle contributions as described in chapter 3.7.

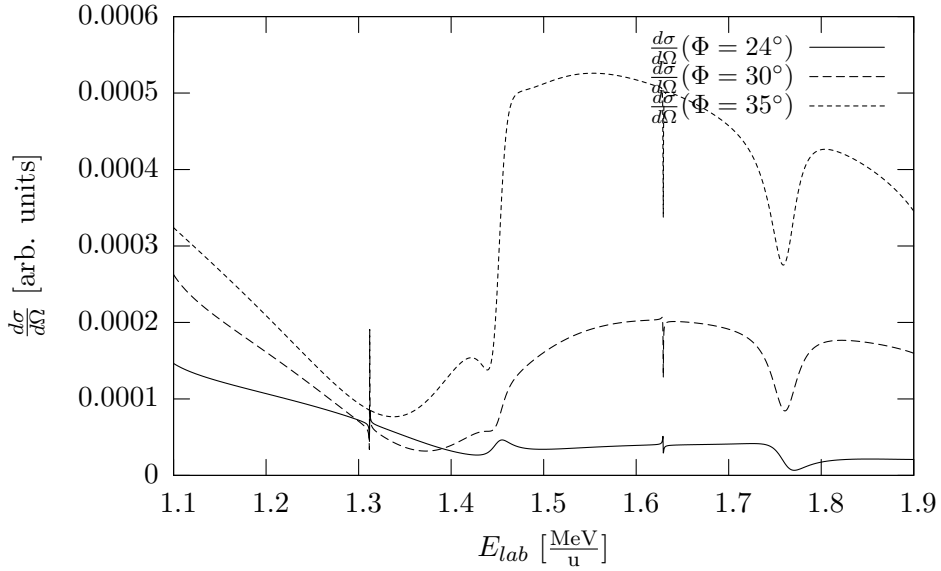

Figure 8: The variation of $\frac{d\sigma}{d\Omega}$ with scattering angle Φ. (Note: the scaling of this curves is not absolute accurate, since the R-Matrix output has been scaled 'manually' into the lab-system of the target atoms, as described in this section.)

3.7 Influence of Monitor Geometry

With regard to the smooth experimental curves, I investigated the accuracy of $\frac{d\sigma}{d\Omega}$ as description for the detected scattering rates. The cross sections calculated by the R-matrix program are valid for one scattering angle, according to the direction of the telescope axis. Therefore, all effects caused by the finite solid angle of the monitor setup are disregarded. Collimator sizes and positions could affect the elastic-scattering spectra, because $\frac{d\sigma}{d\Omega}$ rapidly varies with θ and this variation in turn depends on the beam energy E. The scattering angle of ^{4}He atoms in the laboratory system is referred to as Φ. In order to investigate these variations, I ran the R-matrix program with several angles Φ in the specified ranges of EM1 (51.9°-61.8°) and EM2 (23.2°-36.2°). Some results are plotted in fig. 8, showing the strong fluctuation of $\frac{d\sigma}{d\Omega}$ in the angular range of EM2.

3.7.1 Angle Contributions

It is not sufficient to average the differential cross sections over the angular ranges, because each scattering angle has a different contribution according to the hit proportion of detector surface. That is, the angle contribution functions (called $AC_{EM1}(\Phi)$ and $AC_{EM2}(\Phi)$) are not rectangular functions.

Theoretically, this function could be derived from the detector count spectra (of which two examples are shown in fig. 6), since the energy of elastically scattered ^{4}He atoms is simply determined by the scattering angle

and the beam energy. Unfortunately, this is not a feasible method, because the energy resolution of the SSB detectors is too bad, or there are too many other effects causing broadening of the peak. In EM1 spectra, there is even a double-peak structure visible, that cannot be explained by the θ-dependence of $\frac{d\sigma}{d\Omega}$.

Therefore, the angle contribution functions had to be calculated from the elastic monitor geometry. This has been done in two different ways: With a projector, the range of the hit detector surface has been measured in the two-dimensional drawing shown in fig. 3 and the corresponding for all integer angles in the relevant ranges, and the obtained data could be fitted by the parables shown in fig. 9 (labeled 'fit of meas.'). The functions are noted in appendix C. Also a spreadsheet has been written (with the input parameters: telescope direction, telescope length and collimator sizes) that calculates the contribution of each scattering angle. The result is shown in fig. 9 as well (labeled 'calc.'). In both cases, the minimum and maximum scattering angles differ from those stated before (especially for EM2).

The projector-method seemed to deliver much better elastic scattering spectra. By multiplying $\frac{d\sigma}{d\Omega}$ with the measured angular contributions, the agreement of theoretical and experimental data could be improved by one more step.

However, getting more familiar with the R-matrix program, I have also noticed that it does not deliver $\frac{d\sigma}{d\Omega}$ for the laboratory system of scattered target atoms. The transformation into this frame is necessary for a combination of different scattering angles as it has been made with the angle contribution functions. The output has been scaled 'manually', with the transformed Rutherford cross sections as standard, because they describe the cross sections at low energies.

At least for one detector, EM2, the theoretical curve now agreed well with the experimental results (see fig. 7 (b)). Nevertheless, one has to bear in mind, that the shape of the theoretical graph depends very sensitively on the applied angular contribution function. Concerning EM1, unexplicable deviations were still present in the elastic scattering spectra.

3.7.2 Suspicion of Damage at Elastic Monitor EM1

The calculation of the Rutherford cross sections (in the lab-system of ^{4}He) gave another surprise: The ratio of the Rutherford-scattering cross section for $\Phi = 57°$ and $\Phi = 30°$ was expected to be about 9.5 (Most Rutherford scattered target atoms have a scattering angle of about 90°, corresponding to small scattering angles for ^{12}C). However, the comparison of the scattering rates, scaled to the experimental data of EM1 and EM2, showed, that the (Rutherford-) scattering rate at EM1 was only a third of that at EM2. This is, the count number of EM1 (for all energies) seems to be a factor of 30 too low, compared with EM2. Of course, the longer telescope of EM1 has to be regarded, which results in a smaller solid angle Ω, but this doesn't reduce the factor to less than 20. Herefrom aroused the suspicion that the surface

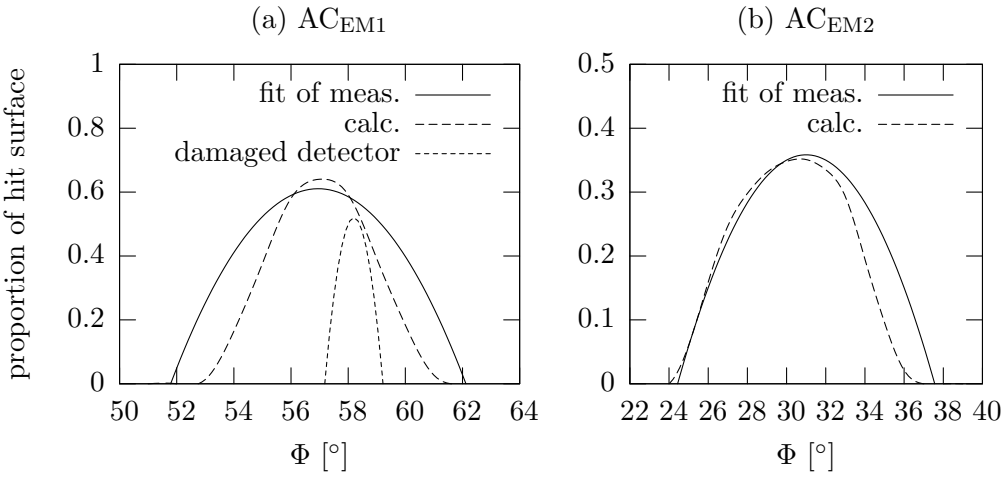

Figure 9: Angle contributions for the Elastic Monitors

of this detector is partly damaged, which would also explain the double-peak structure (and perhaps the large background) in its energy spectra.

I compared $\frac{d\sigma}{d\Omega}$ for several scattering angles with the experimental data and found that an angle contribution from 58° to 59° (also plotted in fig. 9 (a)) would serve very well as a description of the exp. scattering rates (shown in fig. 7 (a)). This is another reason, why EM1 is probably damaged.

The elastic monitors should be tested with an α-source (this is a remaining task) and replaced if necessary. With an intact detector EM1, probably the parabel function for AC_{EM1} (the solid line in fig. 9 (a)) is applicable.

4 Conclusions

By normalizing the elastic scattering data in respect to beam current and target density, smooth spectra could be obtained. The convolution of the theoretical function of $\frac{d\sigma}{d\Omega}(\theta, E)$ with proper angle contribution functions for each detector provided a good description of the elastic scattering rates. The transformation of $\frac{d\sigma}{d\Omega}$ into the lab-system of ^{4}He in a more sophisticated way is another remaining task.

With regard to the angle contribution functions, it should be possible to use the elastic monitors (instead of FCM2) as a primary measurement of the beam current in the target. In any case, the smoothness of the elastic scattering spectra is now sufficient for exposing erranous runs. This can be done in future experiments as well, just by regarding the measured charge state fraction $CSF_{6+}(p, E)$ and accurate data for the target pressure. For the latter, it would be useful to include the manometer SMGC in the data acquisition system.

References

[1] L. Buchmann et al.: Analysis of the total $^{12}C(\alpha,\gamma)^{16}O$ cross section based on available angular distribution and other primary data (Phys.Rev.C 54(1), 1996)

[2] C.E. Rolfs and W.S. Rodney: Cauldrons in the Cosmos (Univ. of Chicago Press, 1988)

[3] D.A. Hutcheon et al.: The DRAGON facility (...): design, construction and operation (Nucl. Instruments & Methods in Phys. Res. A) (see http://dragon.triumf.ca/docs/hutcheon.pdf)

[4] J.M. D'Auria, L. Buchmann: Studies of Elemental Synthesis in Exploding Stars Using DRAGON and TUDA with Radioactive Beams at ISAC (Nucl. Physics News 14(2), 2004) (see http://dragon.triumf.ca/docs/NPN.pdf)

[5] R.E. Laxdal et al.: ISAC at TRIUMF: Recent Achievements and Future Goals (see http://www.triumf.ca/download/lax/isac_status.ps)

[6] W. Liu: Charge State Studies of Heavy Ions Passing through Gas (Master Thesis, 2001) (see http://dragon.triumf.ca/docs/wenjiethesis.pdf)

[7] Yu M Tsipenyuk: Nuclear Methods in Science and Technology (Institut of Physics Publishing, 1997)

[8] Program by J.F. Ziegler and J.P. Biersack (2003) (see http://www.srim.org), the calculation is described in 'The Stopping and Range of Ions in Solids', by J. F. Ziegler, J. P. Biersack and U. Littmark, Pergamon Press (2003)

A Improved Data

Run#	E_{lab} [$\frac{\text{MeV}}{\text{u}}$]	EM1 (57°)	EM2 (30°)	CSF_{6+}	FCM2 [10^{-8} C]	DTF_{HI}	p_{av} [T]	Pre-scaler	CS_{sep}	CS_{in}	Tune
12025	1.7372	98	463	0.443	**16704**	0.736	3.646	5	6	3	-0.75
12027	1.7371	185	830	0.469	**15378**	0.673	3.882	4	6	3	-0.75
12028	1.7372	573	2341	0.445	**44343**	0.660	3.668	4	6	3	-0.75
12029	1.737	769	3004	0.475	**57250**	0.658	3.943	4	6	3	-0.75
12030	1.737	2342	9513	0.471	**187570**	0.638	3.907	4	6	3	-0.75
12031	1.737	514	2063	0.483	**24838**	0.976	4.017	4	6	3	-0.75
12034	1.7552	2273	4330	0.418	**82775**	0.939	3.615	4	6	4	0
12035	1.755	393	882	0.459	**17093**	0.961	3.976	4	6	4	-0.75
12037	1.7549	236	515	0.475	**11661**	0.925	4.116	4	6	4	-1
12038	1.7557	5536	11390	0.348	**13224**	0.956	3.009	0	6	4	-0.75
12043	1.7557	1797	3644	0.348	**3996**	0.954	3.011	0	6	4	-1.25
12045	1.7557	1447	2995	0.346	**3303**	0.953	2.999	0	6	4	-0.9
12047	1.7557	138	290	0.344	**303.4**	0.989	2.974	0	6	4	-1.5
12048	1.7557	7996	15910	0.343	**17514**	0.956	2.972	0	6	4	-1
12059	1.7621	15940	23390	0.440	**20467**	0.952	3.808	0	6	4	-1
12060	1.7622	33550	50020	0.428	**44452**	0.945	3.702	0	6	4	-1
12063	1.8058	5100	7905	0.481	**5815**	0.920	4.168	0	6	4	-1
12064	1.8059	7726	11750	0.471	**9703**	0.817	4.077	0	6	4	-1
12065	1.8059	10570	16110	0.461	**12694**	0.853	3.989	0	6	4	-1
12070	1.4491	24670	13410	0.401	**21750**	0.960	3.526	0	6	3	-1
12072	1.4492	7458	5193	0.387	**7267**	0.970	3.380	0	6	3	-1
12073	1.4489	11770	7226	0.436	**10445**	0.979	3.899	0	6	3	-1
12076	1.4488	7545	4969	0.443	**7027**	0.977	3.978	0	6	3	-1
12078	1.4752	6233	11890	0.450	**7486**	0.988	4.002	0	6	3	-1
12080	1.4752	10140	19100	0.454	**12072**	0.988	4.044	0	6	3	-1
12081	1.4754	23900	44030	0.423	**30388**	0.913	3.710	0	6	3	-1
12082	1.4752	138400	255600	0.444	**179370**	0.882	3.928	0	6	3	-1
12089	1.5154	112400	193700	0.422	**113250**	0.976	3.628	0	6	3	-1
12090	1.5352	182400	322000	0.456	**178620**	0.973	3.956	0	6	3	-1
12093	1.5611	47030	87750	0.464	**47283**	0.983	3.995	0	6	3	-1
12094	1.5611	133500	247700	0.462	**134660**	0.972	3.976	0	6	3	-1
12095	1.5613	133900	246900	0.433	**133380**	0.980	3.687	0	6	3	-1
12100	1.6012	56360	108500	0.458	**61510**	0.926	3.884	0	6	3	-1
12104	1.6381	75120	150500	0.462	**109090**	0.825	3.892	0	6	3	-1
12105	1.6382	67290	133800	0.445	**80989**	0.899	3.728	0	6	3	-1
12106	1.6381	89650	180900	0.461	**104940**	0.924	3.881	0	6	3	-1
12107	1.6332	15140	25300	0.451	**14297**	0.991	3.787	0	6	3	-1
12108	1.6333	235100	381900	0.445	**250310**	0.857	3.728	0	6	3	-1
12110	1.6673	155200	321000	0.443	**196410**	0.900	3.684	0	6	3	-1
12111	1.685	11830	25660	0.474	**16568**	0.837	3.967	0	6	3	-1
12112	1.6851	93450	203000	0.467	**135570**	0.847	3.900	0	6	3	-1
12113	1.6851	54230	118300	0.460	**77249**	0.869	3.832	0	6	3	-1
12114	1.6852	128800	280600	0.446	**185710**	0.857	3.697	0	6	3	-1
12115	1.7229	43670	113700	0.492	**72455**	0.963	4.120	0	6	3	-1
12116	1.4562	26190	45666	0.445	**43876**	0.860	3.989	0	6	3	-1
12117	1.4565	182900	279500	0.405	**285180**	0.896	3.548	0	6	3	-1
12121	1.4562	4952	8611	0.443	**8016**	0.910	3.965	0	6	3	-1
12122	1.4563	7323	12510	0.435	**9585**	0.897	3.877	0	6	3	-1
12123	1.3644	79900	37860	0.412	**123310**	0.954	3.837	0	6	3	-1
12124	1.3647	325300	153400	0.375	**501610**	0.967	3.414	0	6	3	-1
12125	1.2996	145800	201700	0.377	**397350**	0.979	3.622	0	6	3	-1
12126	1.2993	40840	56120	0.406	**108610**	0.974	4.002	0	6	3	-1
12127	1.2222	22010	79740	0.393	**66707**	0.997	4.222	0	6	3	-1
12128	1.2225	40000	145500	0.367	**127040**	0.997	3.810	0	6	3	-1
12129	1.2227	87220	317400	0.351	**283260**	0.996	3.576	0	6	3	-1

Table 1: Improved data for the $^{12}\text{C}(\alpha,\gamma)^{16}\text{O}$ runs. 'DTF_{HI}' means dead time factor for heavy ion detection and 'CS' means charge state. The energy values were calculated for the center of the target cell. All charge state fractions for an incoming charge state $CS_{in} = 4$ are only estimations.

Run#	Statements
12026	Tune 0 ? (all other runs at this energy have a different tune)
12036	Prescaler has been changed during the run
12058	FCM2 problem (not reading in the first half of run)
12066	FCM2 problem (not reading)
12067	q_{in}=4+, despite low energy
12069	Tune did not get applied; see Logbook p. 9-10
12071	FCM2 problem (not reading)
12101	Run sheet incompl.; beam off-center (see Logbook p. 58); diff. energy (p.60)

Table 2: Rejected Runs

B CSD Results

B.1 Carbon

Run	E_{lab}	p	FC1	FC4	FCCH [pnA]			CSF		
#	$[\frac{\text{MeV}}{\text{u}}]$	[T]	[enA]	[pnA]	C^{6+}	C^{5+}	C^{4+}	C^{6+}	C^{5+}	C^{4+}
13521	1.75	5.97	14.30	2.67	1.617	0.914	0.058	0.625	0.353	0.022
13521	1.75	7.92	14.60	2.65	2.333	0.982	0.041	0.695	0.293	0.012
13521	1.75	4.16	13.85	2.63	1.270	1.208	0.147	0.484	0.460	0.056
13521	1.75	2.07	12.65	2.63	0.547	1.456	0.618	0.209	0.556	0.236
13521	1.75	0.80	10.85	2.63	0.083	0.792	1.448	0.036	0.341	0.623
13522	1.6	2.15	9.58	2.30	0.463	1.110	0.368	0.239	0.572	0.189
13522	1.6	4.18	9.76	2.30	0.967	0.920	0.108	0.485	0.461	0.054
13522	1.6	6.10	10.95	2.30	1.250	0.700	0.047	0.626	0.351	0.023
13522	1.6	8.17	11.30	2.30	1.413	0.586	0.036	0.694	0.288	0.018
13522	1.6	7.11	11.10	2.30	1.350	0.650	0.034	0.664	0.320	0.017
13524	1.6	4.98	10.00	2.15	1.042	0.770	0.070	0.554	0.409	0.037
13527	1.6	2.99	10.00	2.17	0.683	1.060	0.200	0.352	0.545	0.103
13527	1.6	1.08	8.30	2.17	0.113	0.830	0.900	0.061	0.450	0.488
13532	1.4	1.06	7.95	2.42	0.132	0.780	0.800	0.077	0.456	0.467
15538	1.4	2.08	8.00	2.40	0.367	1.020	0.375	0.208	0.579	0.213
13534	1.4	3.20	9.00	2.40	0.667	0.940	0.175	0.374	0.528	0.098
13535	1.4	4.08	9.20	2.40	0.817	0.840	0.115	0.461	0.474	0.065
15536	1.4	6.09	9.60	2.40	0.983	0.700	0.063	0.563	0.401	0.036
15537	1.4	7.95	9.30	2.35	1.033	0.620	0.048	0.608	0.365	0.028
15539	1.4	1.55	8.45	2.35	0.267	0.980	0.575	0.146	0.538	0.316
13540	1.45	2.01	10.05	2.50	0.080	0.226	0.083	0.206	0.580	0.214
13540	1.45	4.06	9.71	2.50	0.190	0.184	0.022	0.480	0.465	0.054
13540	1.45	5.92	10.90	2.50	0.248	0.160	0.011	0.592	0.381	0.027
13540	1.45	0.69	8.40	2.50	0.009	0.116	0.255	0.025	0.305	0.670
13541	1.2	2.06	7.68	2.22	0.067	0.182	0.070	0.209	0.571	0.220
13541	1.2	3.06	7.90	2.20	0.098	0.168	0.040	0.321	0.548	0.131
13541	1.2	3.98	8.30	2.20	0.120	0.166	0.028	0.383	0.530	0.088
13541	1.2	5.12	8.40	2.20	0.140	0.166	0.020	0.429	0.509	0.061
13541	1.2	6.28	8.45	2.18	0.143	0.152	0.018	0.458	0.486	0.056
13541	1.2	8.09	8.60	2.17	0.150	0.148	0.015	0.479	0.473	0.048
13542	1.2	0.75	6.60	2.15	0.010	0.100	0.168	0.036	0.360	0.604
13544	1.0	5.35	9.93	2.19	0.543	1.146	0.275	0.277	0.583	0.140
13545	1.0	3.99	9.99	2.22	0.507	1.160	0.308	0.257	0.588	0.156
13546	1.0	3.09	9.84	2.24	0.465	1.188	0.363	0.231	0.589	0.180
13547	1.0	2.08	9.75	2.22	0.527	1.690	0.543	0.191	0.613	0.197
13548	1.0	1.26	9.68	2.21	0.550	1.444	0.800	0.197	0.517	0.286
13549	1.0	0.72	7.89	2.18	0.082	0.904	1.238	0.037	0.407	0.557
13550	0.8	0.62	9.25	2.32	0.062	0.804	1.788	0.023	0.303	0.674
13551	0.8	1.18	9.65	2.29	0.173	0.730	1.360	0.077	0.323	0.601
13552	0.8	2.24	9.75	2.31	0.293	1.606	1.023	0.100	0.550	0.350
13553	0.8	3.56	9.69	2.27	0.328	1.650	0.898	0.114	0.574	0.312
13554	0.8	5.37	9.73	2.24	0.340	1.670	0.880	0.118	0.578	0.304
13555	0.8	7.59	9.74	2.27	0.340	1.688	0.910	0.116	0.575	0.310

Table 3: Charge state distribution of $^{12}C^{3+}$ beam passed through the ^{4}He gas target. Please note: Because of the defect of one charge slit we have used the harp scanner for beam centering. At all measurements with beam energies of 1.45 and 1.2 $\frac{\text{MeV}}{\text{u}}$, the harp scanner has not been removed before reading the FCM2 current, so there has occured beam loss between MD1 and ED1. However, as visible in 3-dim. plots of $CSF_q(p, E)$, this had no bearing on the CSD results.

Polynomial fit for the charge state fraction of C^{6+} (valid for the ranges $3.0\,\mathrm{T} \leq \mathrm{p} \leq 4.5\,\mathrm{T}$ and $1.0\,\frac{\mathrm{MeV}}{\mathrm{u}} \leq \mathrm{E} \leq 1.75\,\frac{\mathrm{MeV}}{\mathrm{u}}$):

$$\begin{aligned} CSF_{6+}(p,E) &= 4.201 \cdot 10^{-4}\ p^3 + 0.1623\ E^3 - 8.782 \cdot 10^{-3}\ p^2E \\ &\quad -7.512 \cdot 10^{-2}\ pE^2 - 3.580 \cdot 10^{-3}\ p^2 - 0.7281\ E^2 \\ &\quad +0.3676\ pE - 0.1779\ p + 0.8362\ E - 0.2839 \end{aligned}$$

with p in unit of T and E in $\frac{\mathrm{MeV}}{\mathrm{u}}$.

B.2 Oxygen

Run #	E_{lab} [$\frac{\mathrm{MeV}}{\mathrm{u}}$]	p [T]	FC1 [enA]	FC4 [pnA]	FCCH [pnA] O^{8+}	O^{7+}	O^{6+}	O^{5+}	O^{4+}
13556	1.0	2.10	3.46	0.55	0.0044	0.103	0.333	0.096	0.0088
13556	1.0	4.18	3.60	0.55	0.0075	0.139	0.317	0.078	0.0065
13556	1.0	6.00	3.65	0.55	0.0088	0.149	0.308	0.078	0.0065
13556	1.0	7.88	3.54	0.55	0.0094	0.153	0.308	0.074	0.0065
13556	1.0	0.72	3.30	0.55	0.0001	0.028	0.258	0.214	0.046
13557	0.75	1.02	3.11	0.55	0.0013	0.022	0.240	0.212	0.055
13557	0.75	1.98	3.24	0.55	0.0006	0.029	0.258	0.198	0.044
13557	0.75	3.99	3.22	0.55	0.0004	0.031	0.260	0.198	0.044
13557	0.75	6.01	3.10	0.55	0.0000	0.032	0.258	0.200	0.044
13557	0.75	7.92	3.19	0.55	0.0000	0.029	0.255	0.200	0.046
13559	0.5	0.37	2.55	0.54	0.0000	0.0006	0.055	0.204	0.205
13560	0.5	0.99	2.70	0.54	0.0000	0.0010	0.068	0.218	0.185
13561	0.5	2.00	2.70	0.53	0.0000	0.0011	0.067	0.220	0.180
13562	0.5	4.16	2.57	0.54	0.0000	0.0010	0.065	0.216	0.183
13563	0.5	7.26	2.52	0.53	0.0000	0.0009	0.060	0.212	0.188

Run #	CSF O^{8+}	O^{7+}	O^{6+}	O^{5+}	O^{4+}
13556	0.008	0.189	0.611	0.176	0.016
13556	0.014	0.253	0.579	0.143	0.012
13556	0.016	0.270	0.560	0.142	0.012
13556	0.017	0.277	0.560	0.134	0.012
13556	0.0002	0.052	0.473	0.392	0.084
13557	0.0024	0.042	0.452	0.400	0.104
13557	0.0012	0.055	0.487	0.374	0.083
13557	0.0007	0.059	0.487	0.371	0.082
13557	0.0000	0.060	0.483	0.374	0.083
13557	0.0000	0.055	0.481	0.378	0.086
13559	0.0000	0.0012	0.118	0.439	0.441
13560	0.0000	0.0021	0.145	0.462	0.392
13561	0.0000	0.0024	0.143	0.470	0.385
13562	0.0000	0.0022	0.140	0.465	0.393
13563	0.0000	0.0019	0.130	0.461	0.407

Table 4: Charge state distribution of $^{12}O^{4+}$ beam passed through the ^{4}He-gas target.

C Angle Contribution Functions

Parabel fit of the measured angle contributions (solid lines in fig. 9):

$$\begin{aligned} AC_{EM1}(\Phi) &= -0.0228763(\Phi/^\circ - 56.9541)^2 + 0.610636 \\ AC_{EM2}(\Phi) &= -0.00832(\Phi/^\circ - 31)^2 + 0.3584 \end{aligned}$$